



Structural Relaxation in Polyanionic Sodium Fluorophosphate Glasses

Courtney Calahoo^{1*}, Jelena Petrovic¹, Quyen Huyen Le¹, Ulrike Werner-Zwanziger², Josef Zwanziger² and Lothar Wondraczek^{1*}

¹ Otto Schott Institute of Materials Research, University of Jena, Jena, Germany, ² Department of Chemistry, Dalhousie University, Halifax, NS, Canada

OPEN ACCESS

Edited by:

Randall Youngman,
Corning Inc., United States

Reviewed by:

Yuanzheng Yue,
Aalborg University, Denmark
Hellmut Eckert,
Universidade de São Paulo São
Carlos, Brazil

*Correspondence:

Courtney Calahoo
courtney.calahoo@uni-jena.de
Lothar Wondraczek
lothar.wondraczek@uni-jena.de

Specialty section:

This article was submitted to
Glass Science,
a section of the journal
Frontiers in Materials

Received: 19 March 2019

Accepted: 24 June 2019

Published: 11 July 2019

Citation:

Calahoo C, Petrovic J, Le QH,
Werner-Zwanziger U, Zwanziger J and
Wondraczek L (2019) Structural
Relaxation in Polyanionic Sodium
Fluorophosphate Glasses.
Front. Mater. 6:165.
doi: 10.3389/fmats.2019.00165

Structural heterogeneity is a common feature of all glasses, however, little is known about the underlying contributions of chemical fluctuations and modulations in free volume in concrete glass forming systems. In this investigation, we relate the dynamics of structural relaxation of $(100-x)\text{NaPO}_3-x\text{AlF}_3$ glasses to their heterogeneous structure as determined from multinuclear magnetic resonance spectroscopic analysis. For this, we evaluate differential scanning calorimetry (DSC) data using the integral isoconversional method to determine the variation in activation energy, E_a , of the glass transition as a function of temperature and conversion progress. Specific heat measurements from DSC allow for the determination of the effective size of the cooperatively rearranging region (CRR). From ^{31}P , ^{19}F , and ^{27}Al NMR, we observe that the introduction of AlF_3 into the NaPO_3 network increases the average connectivity (i.e., the number of heteronuclear $\text{Al}-\text{O}-\text{P}$ bonds), rationalizing the higher E_a determined from the DSC measurements. We find highly constrained regions of $\text{Al}(\text{OP})_4\text{F}_2$ with $\text{Al}-\text{F}-\text{Al}$ cross-linking (high E_a) and, simultaneously, more flexible regions of phosphate chains containing $\text{P}-\text{F}\cdot(\text{Na}^+)_n$ bonds (low E_a); this results in a topologically and dynamically heterogeneous structure as evidenced by the increased variability in E_a with higher AlF_3 content. The decreasing size of the CRR reflects the increased heterogeneity: at low AlF_3 the CRR is large, while at high AlF_3 (high heterogeneity), the CRR is significantly smaller (by a factor of 10^3). Finally, we relate the heterogeneity to other macroscopic properties, such as T_g and mechanical properties.

Keywords: structural relaxation, fluorophosphate glass, ionic glass, structural heterogeneity, thermal analysis, structure-property relationship, NMR spectroscopy, structural analysis

INTRODUCTION

The non-equilibrium structure of glass becomes evident in the relaxation dynamics. Relaxation can occur while heating through the glass transition, or during annealing below the glass transition temperature (physical aging; Vyazovkin, 2015). Since the kinetics of structural relaxation are indicative of molecular mobility and therefore, glass stability, studying the dynamics near the glass transition is of importance for the characterization and fundamental understanding of physical and chemical properties (Greaves and Sen, 2007).

Since the glass is frozen dynamically, the transition preserves the heterogeneity of the liquid state, typically manifest in density fluctuations on the scale of a few nanometers (Ediger, 2000). Macroscopic consequences of structural heterogeneity are found in, e.g., ion mobility

(Greaves and Ngai, 1995), mechanical behavior (Benzine et al., 2018), crystallization (Moesgaard et al., 2010; Zhang et al., 2013), or Rayleigh scattering (Champagnon et al., 2009). During re-annealing of the glass, structural relaxation occurs toward a supercooled liquid via the cooperative motion of ions and molecules (Greaves and Sen, 2007). This process is typically known as α -relaxation; it is characterized by high activation energy (typically hundreds of kilojoules per mole) and stands in contrast to the movement of individual ions, atoms, or molecules (β relaxation). Molecules which are located in highly correlated regions can move only cooperatively, i.e., together with a large number of neighbors, while the molecules in less crowded areas are able to move in a less cooperative manner. The rearrangement of one molecule is only possible if a certain number (N_g) of neighbor molecules also move (Donth, 2001). According to Adam and Gibbs (Adam and Gibbs, 1965), a cooperatively rearranging region (CRR) is defined as a subsystem which, due to thermal fluctuations, can rearrange into another configuration independent of its environment. When the glass relaxes toward the liquid, the overall process generally occurs via convolution of multiple more or less cooperative reactions of structural rearrangement. However, one particular mechanism may dominate the relaxation, depending on temperature or relaxation progress (Vyazovkin, 2015). Near to the glass transition temperature (T_g), structural heterogeneity occurs on the order of a few nanometers in diameter (Duval et al., 2007).

According to the heterogeneous nature of the glass transition, the traditional concept of a constant activation energy [which has already been criticized from a physical point of view (Garn, 1990)] is ill-suited for glass transition kinetics: Garn (1990) has pointed out that a constant activation energy is strictly applicable only to reactions that take place in homogeneous media. In the case of an extremely heterogeneous, hyperquenched CaO-MgO-SiO₂ glass, DSC showed the existence of two separate sub- T_g relaxation peaks corresponding to two dynamically, structurally and energetically different domains (Zhang et al., 2013). However, even for a single-step reaction, the temperature dependence of the physical properties gives rise to variations in energy barrier height and, thus, the activation energy (Vyazovkin, 2016). As a consequence, the glass transition process is represented by a distribution of the activation energies (Moeller et al., 2006). For non-isothermal kinetic analyses, model-fits, and model-free methods are usually employed, whereby model fits are often ambiguous in terms of attributing a given reaction mechanism. For this reason, model-free evaluation routines can be used, such as the isoconversional method which allows for the determination of the effective activation energy as a function of conversion progress without assuming any particular form of the reaction mechanism (Vyazovkin, 2006).

The various isoconversional methods which are available for the evaluation of differential scanning calorimetric data can be distinguished into two groups: Differential isoconversional methods such as proposed by Friedman (2007) typically yield sufficiently accurate values of the effective activation energy, however, they are sensitive to noise in the raw data (Vyazovkin, 2016). Alternatively, integral isoconversional methods (Ozawa, 1965; Flynn and Wall, 1966; Vyazovkin, 2001, 2015) are

significantly less sensitive to noise in the raw data; consequently, they are the most commonly used model-free methods for calculation of the variable activation energy. Common to both groups of methods, they do not yield the reaction model nor the pre-exponential factor. In order to interpret the obtained varying activation energy, a rational must be found from supporting mechanistic data.

Here, we report on the calorimetric investigation of the structural relaxation in fluoride-phosphate mixed-anion glasses of the type $(100-x)\text{NaPO}_3 - x\text{AlF}_3$ (NAPF) using the integral isoconversional method. In those glasses, large amounts of aluminum fluoride can be dissolved (Brow, 1992; Zhang et al., 2007; Le et al., 2017; Bradtmüller et al., 2018). The simultaneous formation of strong Al—O—P bonds and weaker terminal Al—F or P—F bonds reported (Brow, 1992) makes the NAPF system an interesting candidate for studying structural heterogeneity; there are highly constrained, strongly bonded regions (bridging O or F) interspersed among more flexible, less-constrained regions (NBOs or terminal F).

For rationalizing the observation of variable activation energy at the glass transition, we conduct complementary structural investigations of *both* glass former and anion mixing, using ³¹P, ²⁷Al, and ¹⁹F MAS NMR. From DSC analysis, we interpret the variations in activation energy in terms of chemical composition, i.e., changes in dominant intermolecular interactions. Assuming that the activation energy reflects the cooperative dynamics of the glass transition, we examine the activation energy variability as a function of CRR volume. Finally, we relate the distribution of activation energies and average CRR volume to the degree of structural heterogeneity within the glass as determined by NMR.

MATERIALS AND METHODS

In **Table 1** the melting conditions and nominal compositions of the fluorophosphate glasses of this study (NAPF: $(100-x)\text{NaPO}_3 - x\text{AlF}_3$) are given; glasses were prepared using optical-grade raw materials of NaPO₃ and AlF₃. We used platinum crucibles to melt batches of 100 g in a muffle furnace for 1.5 h at 850–1,000°C, followed by homogenization for 2 h at 1,000–1,100°C. Melts were cast into preheated graphite molds and annealed at $T_g + 50^\circ\text{C}$ for 4 h before cooling to room temperature at a rate of about 3–5 K/min. Due to planned NMR experiments, glasses were prepared with a small addition of CuO, 0.2 wt% (where CuO reduces relaxation times), and all types of measurements were made on these doped glasses. As has been thoroughly explored by Möncke et al. (2018), the loss of fluorine at high melting temperatures ($> 850^\circ\text{C}$) is a common problem; as such, we expect that the actual fluorine content is significantly lower than the reported nominal values. All the same, in a binary series such as this, our current and past results indicate a step-wise increase in AlF₃ content (Le et al., 2017).

NMR Experiments

The ³¹P NMR spectra were collected routinely and the experimental parameters are reported in our previous paper (Le et al., 2017). The ²⁷Al ssNMR experiments were conducted on a Bruker Avance NMR spectrometer with a 16.45 T magnet (182.46

TABLE 1 | Nominal compositions (mol %) and synthesis conditions for NAPF glass series.

Glass series	NAPF (100-x)NaPO ₃ – xAlF ₃					
	X	0	10	20	30	40
Synthesis condition	T [°C]	800	850	900	1,000	1,000
	T [h]	1.5	1.5	1.5	1.5	1.5

MHz ²⁷Al NMR Larmor frequency) using our H-F/C-P probe head for rotors of 2.5 mm diameter. The ²⁷Al NMR chemical shift scale was referenced externally against potassium alum at -0.033 ppm as a secondary reference. The ²⁷Al MAS NMR spectra were acquired after a single 0.31 μs pulse (10 degree pulse angle) at 25.00 kHz sample spinning with 0.2 s repetition times accumulating between 1,024 and 4,096 scans depending on the AlF₃ concentration. The short pulse was used to produce quantifiable spectra on quadrupolar nuclei. A spectrum of an empty rotor acquired under identical conditions but summing 18,000 scans characterized the ²⁷Al background signal. This spectrum was subtracted from the sample ²⁷Al NMR spectra after accounting for the different scan numbers accumulated. The chosen chemical shift ranges for integration of aluminum coordinations are the following: Al[4] (29–60 ppm); Al[5] (5–29 ppm); and Al[6] (-63 – 5 ppm).

The ¹⁹F ssNMR experiments were acquired on a Bruker DSX Avance NMR spectrometer with a 9.4 T magnet (400 MHz ¹H, and 376.60 MHz ¹⁹F NMR Larmor frequencies) using our H-F/C-P probe head for rotors of 2.5 mm diameter. The ¹⁹F NMR chemical shift scale was referenced against Teflon at -123.2 ppm as a secondary reference relative to CFCl₃ (MacKenzie and Smith, 2002). The ¹⁹F MAS NMR spectra were acquired with a Hahn-echo sequence ($\pi/2 - \tau - \pi - \text{acquire}$) with $\pi/2$ and π pulse durations of 8.5 and 17 μs, respectively. The echo delay τ was synchronized to one spinner rotation at 25, 23 and 19 kHz MAS spinning frequency ($\tau = 40, 43, 52.6 \mu\text{s}$, respectively). Spin lattice relaxation times, T_1 , were estimated from the 0-crossings of an inversion-recovery experiment with Hahn-Echo detection. The samples were acquired with recycle delays between 5 and 8.4 s equal to or exceeding five times the estimated spin lattice relaxation times, which were shortened by the copper doping. Between 16 and 256 scans were accumulated depending on the ¹⁹F content. The absence of noteworthy background signal was confirmed on the ¹⁹F MAS NMR spectrum of an empty rotor acquired under identical conditions.

Chemical Shielding Calculations

Calculations of the F-19 chemical shieldings were performed using the VASP code (Kresse and Furthmüller, 1996), an implementation of density functional theory using a plane wave basis, periodic boundary conditions, and the projector augmented wave formalism (PAW) (Kresse and Joubert, 1999). The PAW data sets used were those supplied with VASP as the 5.4 release, using the Perdew-Burke-Ernzerhof (PBE) exchange and correlation functional (Perdew et al., 1996). The valence spaces were as follows: F, 2s²2p⁵; Al, 3s²3p; Na, 2s²2p⁶3s; O, 2s²2p⁴; P,

3s²3p³. A 700 eV plane wave energy cut-off was used, and a k point mesh spacing of about 0.02 Å⁻¹. These values were found to be sufficient to converge the shieldings to better than 1 ppm, in these wide band-gap systems. The shieldings themselves were computed using the gauge-including PAW method (GIPAW, Pickard and Mauri, 2001) as implemented in VASP, in which the electron current due to an external magnetic field is computed to first order in density functional perturbation theory and then used to calculate the nuclear magnetic shieldings.

DSC Measurements

Both, specific heat capacity and non-isothermal DSC, measurements were conducted on a Netzsch STA 449 F3 Jupiter equipped with DSC sample holders. Samples were in a bulk form with mass of around 30 mg and one polished surface in order to ensure good contact with the bottom of the employed platinum crucibles and, hence, the thermal sensor. Each measurement was done in inert atmosphere of N₂ with a flow rate of 20 ml/min. Temperature and heat flow calibrations were done for all heating/cooling rates used in this investigation.

In order to erase the initial thermal history, each glass sample was first heated to a temperature of $T_g + 40^\circ\text{C}$, held for 2 min and then cooled down to 60°C at a rate of 20 K/min. The actual DSC scan was subsequently conducted under constant heating rates of 5, 10, 15, and 20 K/min, respectively, up to a peak temperature of $T_g + 60^\circ\text{C}$, followed by cooling back to room temperature at 20 K/min. Each full measurement consisted of two such runs under equivalent conditions. Thereby, the first run was a blank run, with both sample and reference crucibles empty, while the second run had the reference crucible empty and the glass sample in the sample crucible. The temperature program for each run consisted of two subsequent heating and cooling cycles with the same heating/cooling rates. This procedure resulted in four DSC curves per sample, recorded for four different heating rates (5, 10, 15, and 20 K/min).

Specific heat capacity measurements were done in accordance with previous studies (Wondraczek and Behrens, 2007; Wondraczek et al., 2007), using a sapphire crystal as bulk reference material. The specific program consisted of starting at room temperature, then heating up to 40°C, holding for 30 min to equalize the temperature on the samples and furnace, then heating up to $T_g + 60^\circ\text{C}$ with a heating rate of 20 K/min, holding at $T_g + 60^\circ\text{C}$ for another 30 min and finally cooling back to room temperature.

RESULTS

Structure Determination

In order to understand the thermal relaxation processes, the glass structure was analyzed by ³¹P, ¹⁹F, and ²⁷Al MAS NMR. Although the ³¹P NMR spectra have partially been reported elsewhere (Le et al., 2017), we believe the analysis to be pertinent to the discussion here. As shown in **Figure 1**, the ³¹P NMR spectrum of pure NaPO₃ is dominated by the expected single peak at ~-20 ppm (assigned as Q²_{0Al}) with a small contribution near -8 ppm (Q¹_{0Al}). Upon the introduction of 10 mol% AlF₃, two new peaks appear; a peak upfield of each the Q¹_{0Al} and Q²_{0Al} peaks

at -14 and -26 ppm, respectively. Given that aluminum is an intermediate glass former and similar literature (Le et al., 2017), we assign these new peaks to Q^1_{1Al} and Q^2_{1Al} , respectively. In

this paper, we follow the terminology used by Bradtmüller et al. (2018): $Q^n m$ notation is the typical Q^n notation, with n being the number of homonuclear phosphate bonds and m being the number of aluminum neighbors, whereas in the $P^q m$ notation, q refers to number of total bridging oxygens (P or Al). For the 10 and 20 mol% AlF_3 , the peaks with one aluminum neighbor (Q^1_{1Al} and Q^2_{1Al}) grow in at the expense of the Q^1_{0Al} and Q^2_{0Al} peaks, and commensurately with the amount of AlF_3 in the glass.

Figure 2 displays clearly the evolution of the Q^n_m species with increased AlF_3 . For compositions with ≥ 30 mol% AlF_3 , a structural change occurs, where now additional AlF_3 results in the formation of Q^1_{1Al} species only, with Q^2_{1Al} species remaining constant (Q^1_{0Al} and Q^2_{0Al} continue to decrease). Although the four peaks overlap, the area fractions show the expected monotonic exchange between the Q^n species with and without aluminum neighbors. Moreover, the trends match those of Bradtmüller et al. (2018) found for the same glass series, including the increase and then subsequent decrease of the Q^1_{0Al} species. The exact fitting ^{31}P NMR parameters can be found in **Table 2**.

The major advantage of using the P^q_m (q refers to number of total bridging oxygens, P or Al) notation is that we can monitor the connectivity changes in the glass; we observe that although the homonuclear Q^n species, i.e., $P-O-P$ bonds, are decreasing, they are being replaced with equal amounts of heteronuclear $P-O-Al$ bonds. For example, when 10–20 mol% AlF_3 is present in the glass, P^2_{0Al} is being replaced with roughly equal amounts of P^1_{0Al} , P^2_{1Al} , and P^3_{1Al} , summing to only small changes in the number of bridging oxygens connected to the phosphate network. For >30 mol% of AlF_3 , P^2_{0Al} tetrahedra are being replaced with more P^3_{1Al} species than P^1_{0Al} (we are ignoring the increase in P^2_{1Al} , since number of BO is the same). Consequently, the total number of bridging oxygens per phosphate tetrahedron is actually increasing for ≥ 30 mol% AlF_3 .

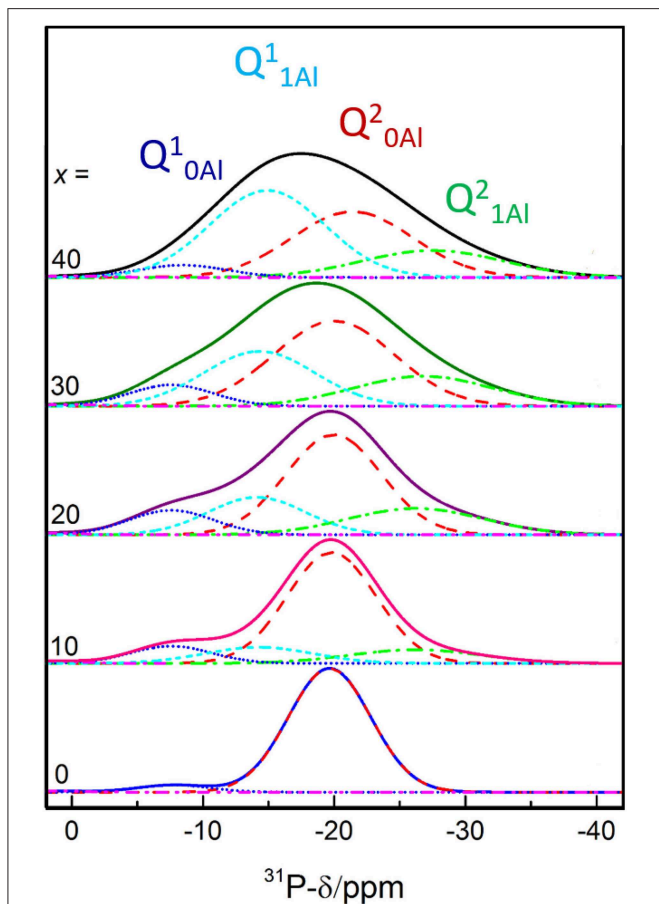


FIGURE 1 | ^{31}P MAS NMR spectra deconvolutions. Modified and reproduced from Le et al. (2017).

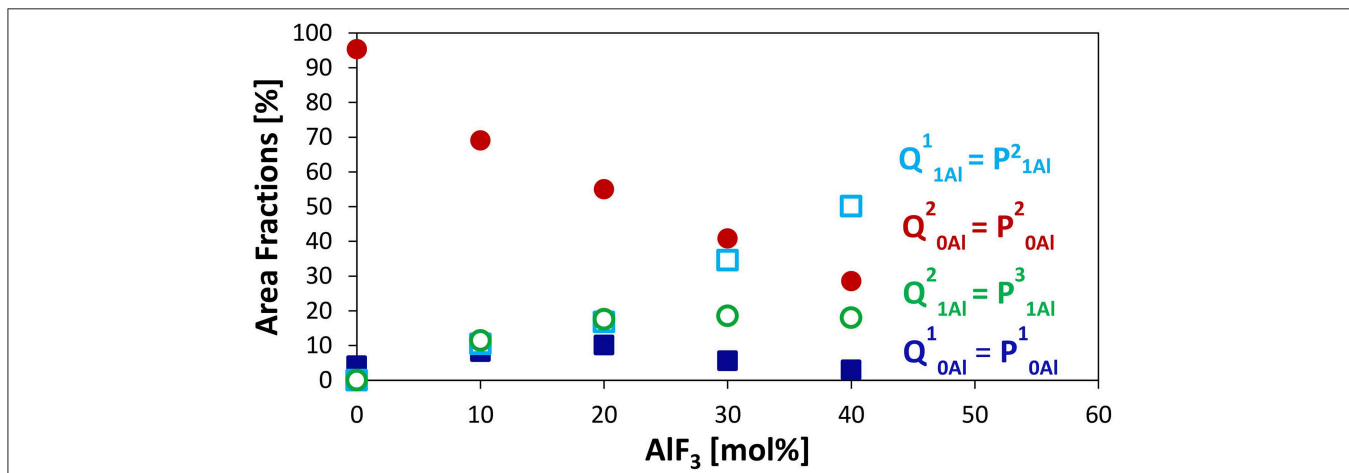
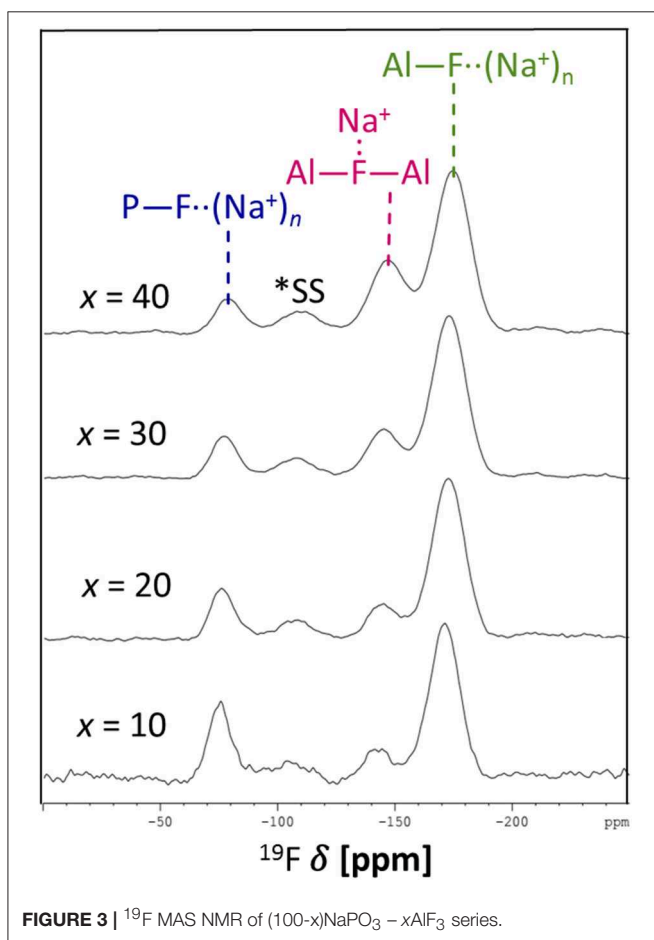


FIGURE 2 | Area Fractions of phosphate $Q^n m$ species (n = number of P neighbors, m = number of Al neighbors) or $P^q m$ (q refers to number of total bridging oxygens, P or Al) from ^{31}P MAS NMR.

TABLE 2 | ^{31}P NMR shifts NMR parameters of $(100-x)\text{NaPO}_3 - x\text{AlF}_3$ series.

X	Q^0			$\text{Q}^1_{0\text{Al}} = \text{P}^1_{0\text{Al}}$			$\text{Q}^1_{1\text{Al}} = \text{P}^2_{1\text{Al}}$			$\text{Q}^2_{0\text{Al}} = \text{P}^2_{0\text{Al}}$			$\text{Q}^2_{1\text{Al}} = \text{P}^3_{1\text{Al}}$		
	δ	fwhm	Area	δ	fwhm	Area	δ	fwhm	Area	δ	fwhm	Area	δ	fwhm	Area
	[ppm]	[ppm]	[%]	[ppm]	[ppm]	[%]	[ppm]	[ppm]	[%]	[ppm]	[ppm]	[%]	[ppm]	[ppm]	[%]
0	1.5	5	0.5	-7.8	6.5	4	-	-	-	-19.7	7.4	95	-	-	-
10	1.5	5	0.8	-7.6	7.3	8	-14.3	9.8	10	-19.8	8	69	-26.2	11.8	11
20	1.5	5	0.6	-7.6	7.5	10	-14.1	8.6	17	-20.0	8.7	55	-26.2	12.2	18
30	0.5	5.5	0.5	-7.6	8	6	-14.3	10.9	35	-20.5	10	41	-26.8	12.5	19
40	0	6	0.4	-7.6	9	3	-15.1	11.4	50	-21.6	11	29	-26.8	12.9	18

Modified and reproduced from Le et al. (2017).

**FIGURE 3** | ^{19}F MAS NMR of $(100-x)\text{NaPO}_3 - x\text{AlF}_3$ series.

The ^{19}F NMR spectra in **Figure 3** reveal three types of fluorine in the glass, i.e., terminal phosphorus-bound $[\text{P}-\text{F}\cdot(\text{Na}^+)_n]$, bridging $\text{Al}-\text{F}-\text{Al}$, and terminal aluminum-bound $[\text{Al}-\text{F}\cdot(\text{Na}^+)_n]$ found at -75 , -148 , and -172 ppm, respectively. The assignments are based on NMR studies of similar glass systems and double resonance NMR experiments, which showed a lack of $\text{Al}-\text{F}-\text{P}$ bonds (Le et al., 2017; Bradtmüller et al., 2018). These assignments are validated further by calculated

TABLE 3 | Computed ^{19}F shifts in various crystal models.

Compound	Site	δ_{iso} [ppm]	Nearest Neighbors
AlF_3	F1	-172	2 Al
Na_3AlF_6	F1	-191	1 Al, 2 Na
	F2	-191	1 Al, 2 Na
	F3	-191	1 Al, 2 Na
$\text{Na}_5\text{AlF}_2(\text{PO}_4)_2$	F1	-170	1 Al, 4 Na
NaAlFPO_4	F1	-147	2 Al, 1 Na
$\text{Na}_2\text{PO}_3\text{F}$	F1	-68	1 P, 1 Na
	F2	-74	1 P, 1 Na

Shifts are referenced such that the computed of AlF_3 appears at -172 ppm, as it does experimentally when referenced to neat CFCl_3 ¹.

TABLE 4 | ^{19}F chemical shifts of $(100-x)\text{NaPO}_3 - x\text{AlF}_3$ series.

	$\text{Al}-\text{F}\cdot(\text{Na}^+)_n$	$\text{Al}-\text{F}-\text{Al}$	$\text{P}-\text{F}\cdot(\text{Na}^+)_n$
AlF_3	CS [ppm]	CS [ppm]	CS [ppm]
10	-171.4 ± 0.5	-148 ± 6	-74.7 ± 0.3
20	-172.7 ± 0.1	-146 ± 2	-75.6 ± 0.1
30	-173.1 ± 0.1	-147 ± 2	-76.7 ± 0.5
40	-174.5 ± 0.1	-147.2 ± 0.5	-78.2 ± 0.3

^{19}F NMR chemical shifts for various crystalline compounds (**Table 3**). These calculations reveal that both Na^+ neighbors and phosphate next-nearest neighbors change the ^{19}F chemical shifts of pure AlF_3 significantly: sodium coordination changes the ^{19}F chemical shift from -172 ppm ($\text{Al}-\text{F}-\text{Al}$) in crystalline AlF_3 to -191 ppm for terminal $\text{Al}-\text{F}\cdot(\text{Na}^+)_2$, in Na_3AlF_6 . Yet the further addition of phosphate moves the ^{19}F shift back to -170 ppm for terminal $\text{Al}-\text{F}\cdot(\text{Na}^+)_4$ in $\text{Na}_5\text{AlF}_2(\text{PO}_4)_2$ and back to -147 ppm for bridging $\text{Al}-\text{F}-\text{Al}$ with 1 Na^+ neighbor, in NaAlFPO_4 . The lack of intensity in the ^{19}F spectra at -191 ppm, the computed chemical shift of Na_3AlF_6 , indicates that no

¹The near neighbors to fluorine were determined based on a cut-off of 2.35 \AA , with the exception that the fourth Na in $\text{Na}_5\text{AlF}_2(\text{PO}_4)_2$ is slightly farther, at 2.45 \AA .

TABLE 5 | ^{19}F intensities of $(100-x)\text{NaPO}_3 - x\text{AlF}_3$ series.

	Al—F·(Na ⁺) _n	Al—F—Al	P—F·(Na ⁺) _n
AlF ₃	Int. [%]	Int. [%]	Int. [%]
10	68 ± 2	10 ± 4	22 ± 6
20	70 ± 2	16 ± 2	14 ± 3
30	67 ± 2	20 ± 3	13 ± 5
40	64 ± 2	29 ± 3	8 ± 2

“islands” of Al, F, and Na exist; the chemical shifts found in these glasses correspond to crystals containing phosphate. Also, these shifts indicate that fluorine is always associated with at least one sodium, even bridging fluorines, which may indicate a preference for F·(Na⁺)_n association.

^{19}F NMR spectra collected at three different MAS spinning speeds were fitted using the *dmfit* program (Massiot et al., 2002), accounting for the respective spinning sidebands and their results are given in **Tables 4, 5**.

Figure 4 shows the progression of fluorine types with further addition of AlF₃ to NaPO₃. Within the uncertainty of the peak deconvolution, the relative concentration of Al—F·(Na⁺)_n stays constant, however, with increasing AlF₃ and correspondingly decreasing NaPO₃ content, P—F·(Na⁺)_n is replaced with bridging Al—F—Al (w/one Na⁺ neighbor). This result indicates that as more aluminum is available connectivity increases between the aluminum atoms: at high AlF₃ content ($x = 30, 40$ mol%), there are significant amounts of bridging Al—F—Al bonds, ~17% and ~24%, respectively. The increase in bridging oxygens per phosphate and appearance of Al—F—Al bonds is likely caused by the decrease of sodium available; P and Al want to form four and six bonds, respectively, but are forced to bond to neighboring glass formers, rather than form non-bridging oxygens or terminal fluorines. It is also worth noting that initially when terminal P—F·(Na⁺)_n bonds are prevalent (high sodium), P¹_{0Al} and P³_{1Al} species increase (**Figure 2**), but at low NaPO₃ mol%, when P—F·(Na⁺)_n bonds are only a small structural contribution, P¹_{0Al} and P³_{1Al} peaks stop growing in; this similarity in trends demonstrates how aluminum fluorine initially adds to the phosphate backbone (P¹_{0Al} and P³_{1Al} species) when sodium is present until Al—F—Al bonds begin to dominate and only P²_{1Al} forms.

The ^{27}Al NMR spectra in **Figure 5** reveal that the aluminum site is to a high percentage octahedral (order of and larger than 90%), with a small variation between Al[5]- and Al[4]-fold sites. Given the low intensities of Al[5] and Al[4] coordinations, integration was fixed to a chemical shift range based on the 60NaPO₃-40AlF₃ sample, shown in **Figure 5**; our final values are given in **Table 6**. These values agree with the descriptions reported elsewhere on this same glass series: Bradtmüller et al. (2018) demonstrate that at low AlF₃ content, all the aluminum is 6-fold coordinated and only at high amounts of AlF₃ (40 mol%) are small amounts of 5-fold (8%) and 4-fold (1%) aluminum present. Similarly, Brow (Brow, 1992) observed only one central

peak at -10 ppm in the ^{27}Al NMR spectra of this glass series, without any evidence for Al[4] or Al[5].

Bradtmüller et al. (2018) complete a comprehensive structural study giving many insights to the role of AlF₃ in these glasses. One major conclusion is that the fluorine is uniformly distributed throughout the glass structure, i.e., no AlF₃-like regions are formed. Using the 2nd moments from several nucleus pairs of double resonance NMR experiments, the authors determine that on average Al[6] is coordinated by four phosphorus and two fluorine atoms, Al(OP)₄F₂. Given the similarity in our NMR data as well as phase-pure XRD and optical microscopy results, we also conclude that our glasses contain Al(OP)₄F₂ and do not exhibit phase separation.

Brow et al. (1993) have measured and predicted the distribution of Al[4], Al[5], and Al[6] for a related glass system without fluoride, (1-x)NaPO₃ - xAl₂O₃. They found that the average Al coordination decreased from six to four as the Al/P ratio increased; specifically, only Al[6] was found at low Al/P, ≤ 0.3 , while Al[4] dominates at higher Al/P, ≥ 0.6 . The Al/P ratio of our glass series ranges from 0.1 to 0.7, yet no significant differences in Al-speciation are observed between samples, i.e., no dependence on amount of AlF₃ is found, indicating that fluorine is affecting the glass structure in a different way compared to oxygen.

The strong effect of fluoride addition upon Al coordination can be seen in **Figure 6**, where fluoride content clearly favors 6-fold aluminum at any Al/P ratio. Similar to our results, Zhang et al. (2007) found for sol-gel-derived glasses along the composition lines Na/Al/P/F 2:x:2:1, 2:2:x:1, 2:2:2:x, and x:2:2:x, respectively, that both low Al/P (< 1) and high F/Al (or F/P) ratio were associated with increased fraction of Al[6]. The Al/P ratio still plays a role: at lower Al/P ratio, less fluorine drastically increases the average Al coordination, which agrees well with our ^{27}Al NMR data. If we compare [F]/[Al+P] ratios for Zhang et al. (2007) and our glass system (indicated by degree of shading in **Figure 6**), all of our samples have higher [F]/[Al+P] ratios (and therefore higher proportion of Al[6], with the exception of the 90NaPO₃-10AlF₃ sample, which also has the lowest Al/P ratio). These two factors, Al/P ratio and fluorine content, are the reason we see nearly no variation in Al speciation, unlike the corresponding (1-x)NaPO₃ - xAl₂O₃ series.

The next several structural figures use valence unit [V.U.] theory (Bunker et al., 1991) to understand the driving forces behind the propensity of aluminum to form Al[6] in the presence of fluorine. Valence unit [V.U.] theory proposes that strong cations have V.U. equal to their valence which are shared by the number of bonds they form, i.e., tetrahedral P⁵⁺ has 5 V.U. shared among four bonds. Additionally, oxygen bonds must sum up to 2 V.U., while modifying ions are more fungible (0.1-0.4 V.U. each). Due to the chemical complexity of our system, rather than finding crystals of corresponding composition, we have decided to focus on the fluoride bonding between aluminum and phosphorus. Brow et al. (1993) have used valence bond theory to explain the bonding in aluminophosphate glasses, specifically the equilibrium of Al[4] and Al[6] units as a function of Al/P. **Figure 7A** demonstrates that at low Al/P, ≤ 0.3 , the fluoride bond in Al[4]—F—Al[4] is overbonded. Moreover, in

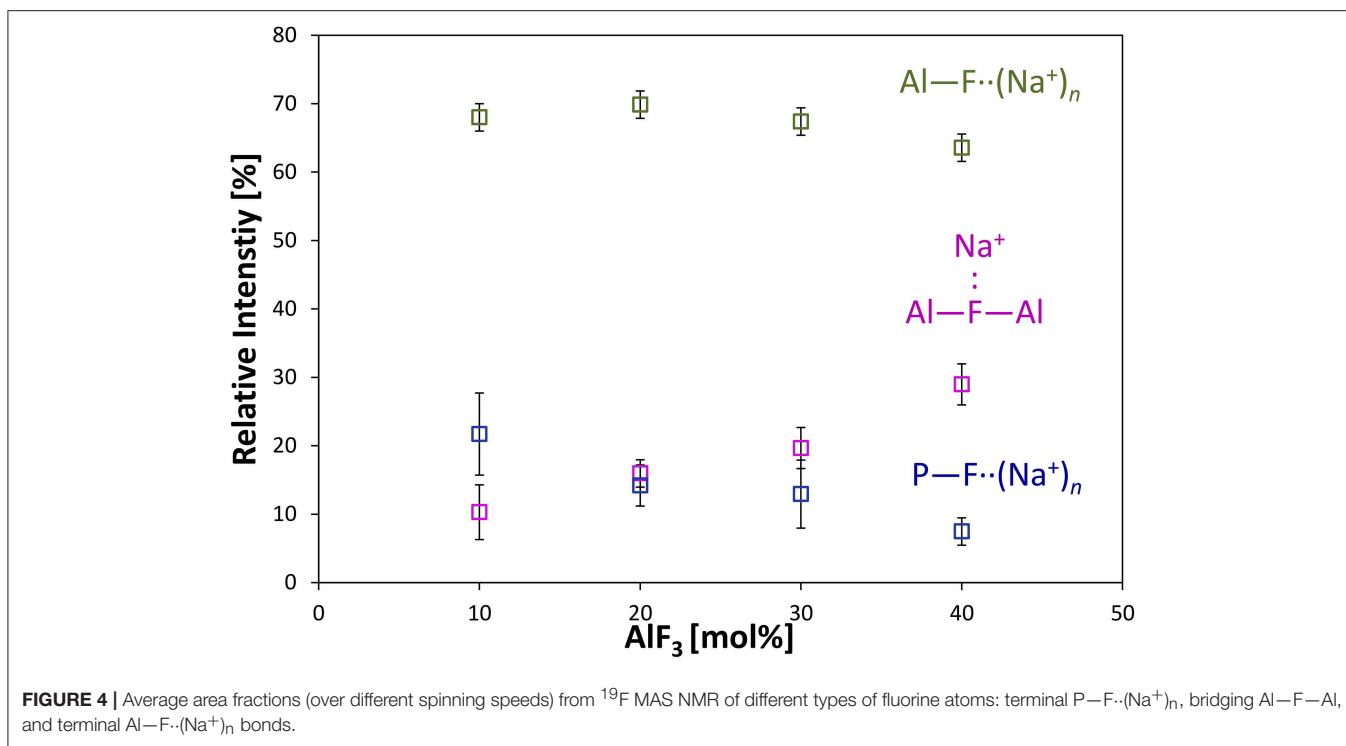


Figure 7B, we observe at the same low Al/P ratio, fluorine is overbonded in P—F—Al[4] and energetically unfavored (even when the NBO and terminal F possess maximum ionicity, *blue values*). In fact P—F·(Na⁺)_n bonds are much preferred and in agreement with the ¹⁹F NMR results: at low Al/P, 10–20 mol% AlF₃, P—F·(Na⁺)_n bonding is prevalent. Indeed, the experimental and calculated ¹⁹F chemical shifts indicate that fluorine, even bridging Al—F—Al bonds have at least one coordinated Na⁺, with terminal fluorines likely requiring more Na⁺ partners; as such, we assume that every terminal fluorine has one Na⁺ contributing 1/6 V.U.

On the one hand, **Figure 7C** clearly indicates the high stability of the bridging fluoride in Al[6]—F—Al[6], with it being preferred over P—F·(Na⁺)_n once sufficient aluminum is available at higher Al/P, 30–40 mol% AlF₃ (¹⁹F NMR). Yet we know that P—F—Al[6] is still not formed: **Figure 7D** proposes that the high electron density (1.8 V.U.) on two NBOs of the phosphate tetrahedra is unstable. In metaphosphate the maximum V.U. on the two NBOs is 1.5 (which can also be intraconverted into 2.0 and 1.0 V.U. or a double and single bond, respectively), thus there is likely a resonance stabilization which cannot be achieved in **Figure 7D**.

Finally, we find it interesting that at low phosphate content, the aluminum coordination is significantly less sensitive to fluorine content; even at the same [F]/[Al+P], the average aluminum coordination is five rather than six observed in Zhang's data (Zhang et al., 2007). **Figure 8** indicates that terminal fluorine have more flexibility in their valence (compared with bridging anions), therefore, they can compensate to ensure the bridging fluorine in Al—F—Al is not overbonded. There appears

to be a large difference in Al/P of 0.67 and Al/P of 1.0, yet as it is always associated with terminal fluorines, the amount of sodium also plays a significant role; when an aluminum can have at least two terminal fluorines it can remain as Al[4] (right side), however, if two P—O—Al bonds are formed (low sodium), then the aluminum prefers Al[6] to accommodate more bridging oxygens (left side).

Thermal Analysis

Examples of endothermic peaks corresponding to the glass transition in NAPF glass ($x = 20$), using heating rates of 5, 10, 15, and 20 K/min, are shown in **Figure 9**. It is evident, from **Figure 9**, that the glass transition temperature (T_g) shifts to higher values with increasing heating rate, illustrating the kinetic nature of the glass transition.

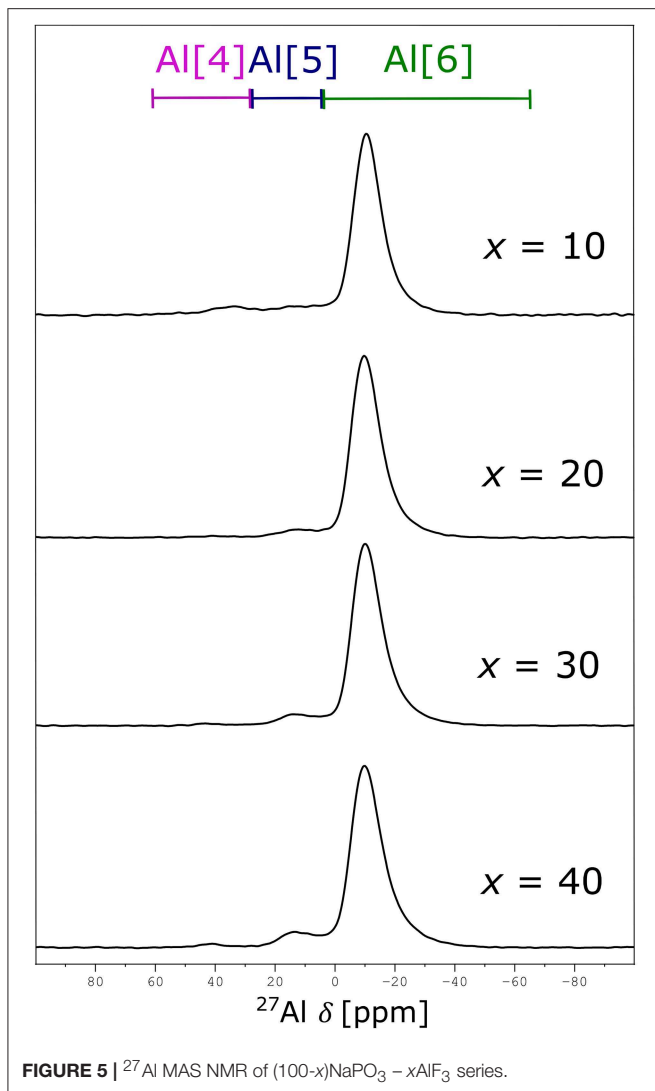
In order to estimate the activation energy as a function of the extent of conversion (α), the integral isoconversional method proposed by Vyazovkin (2015) was applied to the non-isothermal DSC data. Here, variable activation energies (E_α) are calculated by minimizing the function:

$$\Phi(E_\alpha) = \sum_{i=1}^n \sum_{j \neq i}^n \frac{J[E_\alpha, T_i(t_\alpha)]}{J[E_\alpha, T_j(t_\alpha)]} \quad (1)$$

with the integral $J[E_\alpha, T(t_\alpha)]$

$$J[E_\alpha, T_i(t_\alpha)] \equiv \int_{t_\alpha - \Delta\alpha}^{t_\alpha} \exp\left[\frac{-E_\alpha}{RT_i(t)}\right] dt \quad (2)$$

In Equation 2, $T_i(t)$, $i = 1 \dots n$, is a set of arbitrary temperature programs and R is the universal gas constant. The method relies



on direct numerical integration without any approximations. In the next step, the progress of conversion is defined,

$$\alpha = \frac{(\Phi - \Phi_g)|_T}{(\Phi_l - \Phi_g)|_T} \quad (3)$$

where Φ is the heat flow at a given temperature T , and Φ_l and Φ_g represent heat flow values for the liquid and glass phases extrapolated to the same temperature T (inset of **Figure 9**).

The application of the aforementioned procedure results in α vs. T curves (**Figure 10**). The endothermic overshoot which is observed during heating gives rise to α -values which are formally higher than 1, however, the iso-conversional calculations for measurements performed on heating require only the ascending part of the α vs. T curves in the limit of $\alpha = 1$.

The activation energies as a function of both conversion extent and temperature are shown in **Figure 11**. The E_α vs. α and E_α vs. T representations are linked to each other because they are two projections of the same line that cuts

TABLE 6 | Chemical shift ranges and integration of $(100-x)\text{NaPO}_3 - x\text{AlF}_3$ series from ^{27}Al MAS NMR.

	Range Integrated Over [ppm]		
	Start	End	
Start	60.2	29.4	5.1
End	29.4	5.1	-63.3
Relative Intensity [%]			
%AlF ₃	Al[4]	Al[5]	Al[6]
10	5	7	88
20	1	4	95
30	1	6	93
40	2	8	91

The uncertainties of all the relative intensities is $\pm 2\%$.

through the three-dimensional surface $E(\alpha, T)$. The line is determined by the α vs. T trace, which is simply a kinetic curve measured at a given heating rate (Vyazovkin, 2018). Based on the data presented in **Figure 11**, we find that the reduction of $\text{NaPO}_3/\text{AlF}_3$ ratio leads to an increase in E_α values, as well as an increase in the range of activation energies with conversion progress. Addition of 10 mol% AlF_3 causes a small but progressive change in E_α , but not in the range of activation energies. Activation energy in these glasses ($x = 0, 10$) can be considered as constant during the glass transition process, which according to Vyazovkin (2018) can be interpreted as an effectively single-mode relaxation, characterized by an almost constant degree of molecular cooperativity. The near-constant activation energy typically indicates that the rate of a multistep process is either limited or dominated by the rate of one step. When more AlF_3 is added, a distinct peak in E_a develops indicating a pronounced multi-mode relaxation process. The activation energy of the lowest process is equal to that at low AlF_3 content, yet the highest-energy step increases significantly, signifying that a different, higher-energy process is being introduced.

The characteristic volume of the cooperatively rearranging region (CRR) at the glass transition temperature (V_ξ) can be obtained from calorimetric data (Donth, 1982):

$$V_\xi = \xi^3 = \frac{k_B T_g^2 \left(\frac{1}{c_V^{\text{glass}}} - \frac{1}{c_V^{\text{liquid}}} \right)}{\rho (\delta T)^2} \quad (4)$$

where, ξ represents characteristic length (size of CRR), T_g is the glass transition temperature, c_V is the specific heat at constant volume, ρ is density of the sample, k_B is the Boltzmann constant and δT is the average temperature fluctuation of an average CRR. Specific heat capacity, c_V , is a function of the structure of the material itself and depends on the number of degrees of freedom of motion that are available; the larger the number of degrees of freedom available to the particles of the material, the larger the specific heat capacity of the material. Kinetic energy of the particles in the material, i.e., translation and rotation of polyatomic molecules, is only one of the many possible types of degrees of freedom which manifests as a temperature change; some thermal energy may also be stored as the potential energy

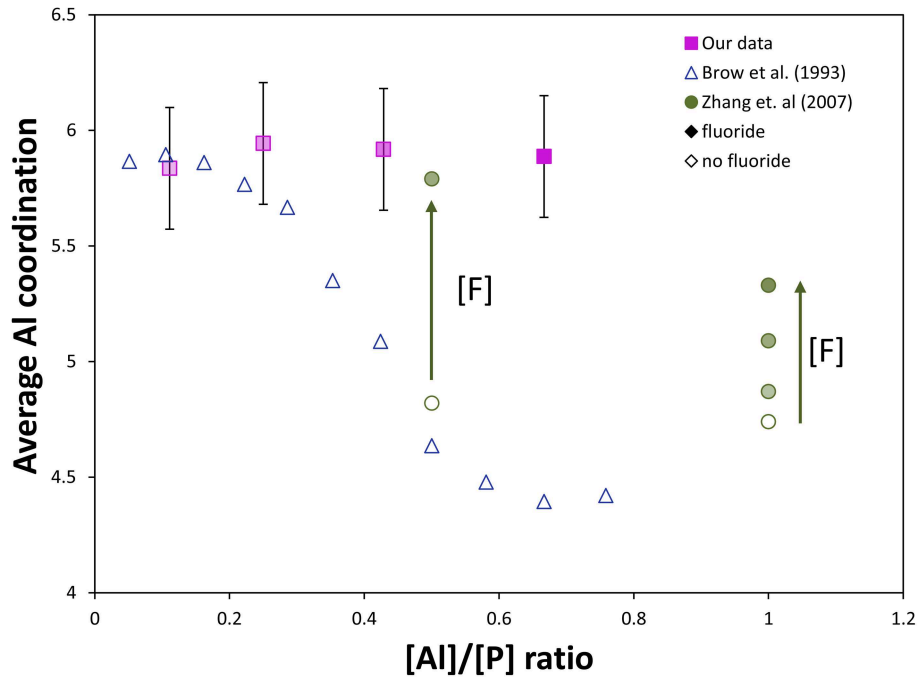


FIGURE 6 | Comparison of our NMR data to literature NMR data from Brow et al. (1993) and Zhang et al. (2007, 2013). Effect of [Al]/[P] ratio and fluorine content on the average Al coordination in aluminophosphate and fluoroaluminophosphate series (completely shaded markers have the most fluoride, $[F]/[Al+P] = 1.2$, and unshaded markers have no fluoride content, $[F]/[Al+P] = 0$). Without fluorine, substantial Al[6] only forms at very low $[Al]/[P]$, ≤ 0.3 . The effect of fluorine content on the Al coordination can be observed: addition of fluoride ($[F]/[P] = 0.5$) forces most Al content into Al[6] despite a much higher $[Al]/[P]$ (~ 0.5) compared with only aluminophosphate, while at sufficiently high $[Al]/[P]$ (~ 1), much more fluoride content can be added without forcing all aluminum into 6-fold coordination (some remains as Al[4] and Al[5]).

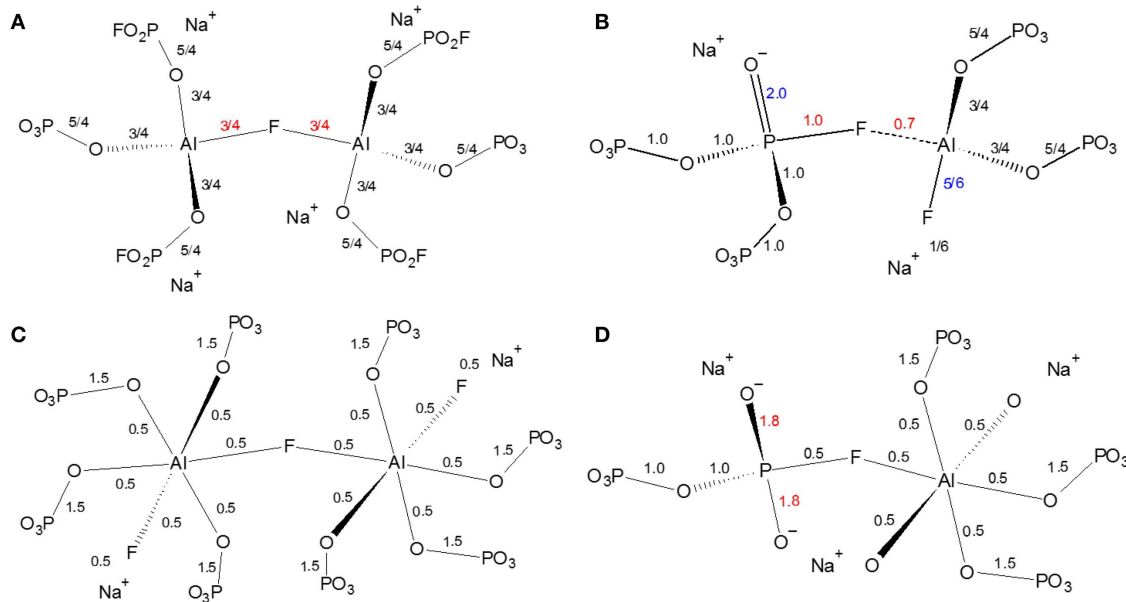
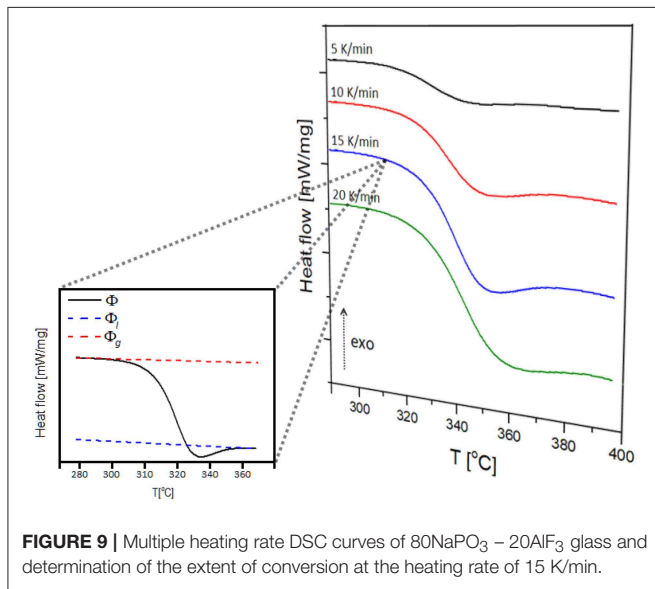
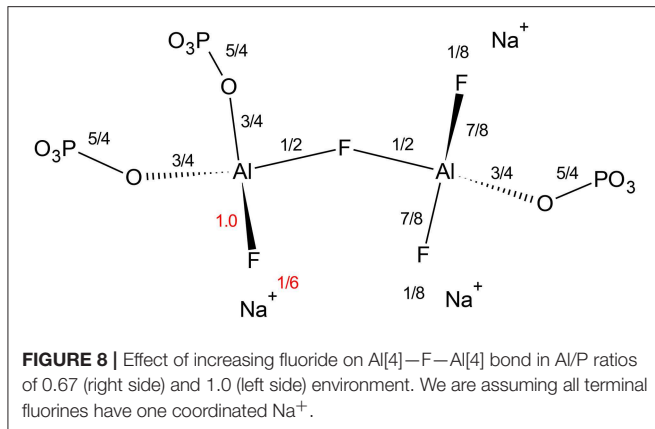


FIGURE 7 | Effect of fluoride in fluoroaluminophosphate glass in phosphate-rich (low Al/P ratio, 0.3) environment **(A)** instability of Al[4]—F—Al[4] bond; **(B)** Instability of P—F—Al[4] bond; **(C)** Al[6]—F—Al[6] bond; **(D)** Instability of P—F—Al[6] bond.

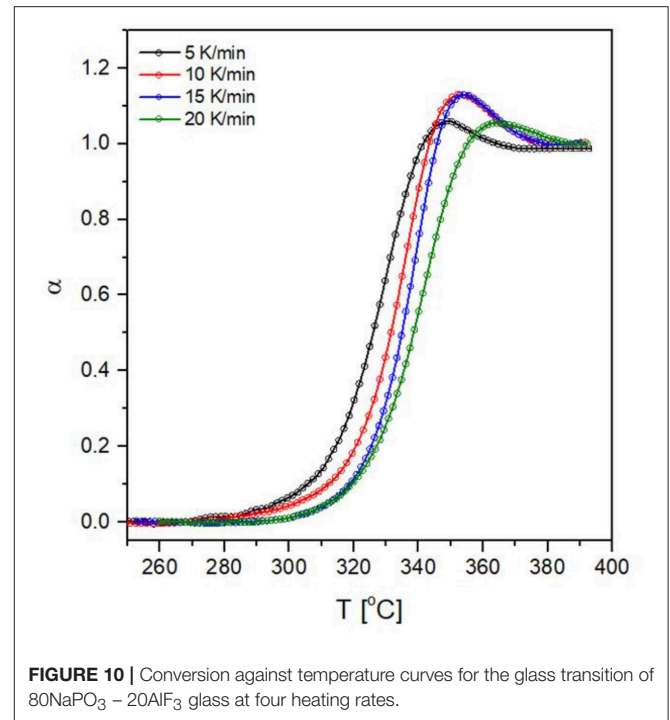


associated with higher energy modes of vibration, often occurring in interatomic bonds in a glass. These two types of energy, kinetic and potential, represent the degrees of freedom of motion which classically contribute to the heat capacity of a thermodynamic system.

Reliable values of $\Delta(1/c_p)$ and δT can be calculated according to Hempel et al. (2000) (Figure 12):

$$\Delta(1/c_v) = \left(\frac{1}{c_v}\right)^{glass} - \left(\frac{1}{c_v}\right)^{liquid} \approx \left(\Delta\frac{1}{c_p}\right) \approx \left(\frac{\Delta c_p}{c_p^2}\right) \left(1 + \left(\frac{1}{4}\right) \left(\frac{\Delta c_p}{c_p}\right)^2 + \dots\right) \quad (5)$$

where c_p and c_v are specific heats (J/mol·K) at constant pressure and volume, respectively. δT represents the mean-square temperature fluctuation of one average CRR, and it is, in the case of specific heat measurements upon



heating, calculated as Hempel et al. (2000):

$$\delta T = \frac{\Delta T}{2.5} \quad (6)$$

Since our specific heat measurements were done under constant pressure, the approximation $\Delta c_p \approx \Delta c_v$ was made in Equation 5 in order to calculate the characteristic volume of the CRR (Equation 4). Previously published Δc_p and Δc_v values (O’Reilly, 1977) were used to calculate a correction factor, S , determined from four small-molecule glass formers and 14 polymers (Hempel et al., 2000):

$$S \equiv \frac{\Delta(1/c_v)}{\Delta(1/c_p)} = 0.74 \pm 0.2 \quad (7)$$

where ± 0.22 is the standard deviation. All V_ξ values (Figure 13) are corrected by $S = 0.74$.

Taking the variability of activation energy as the difference between its minimum and maximum values, we find a relationship between activation energy variability and CRR volume (Figure 13): the activation energy variability decreases exponentially with increasing CRR volume.

DISCUSSION

To better visualize the changes in the phosphate network with increasing AlF₃ content, we begin with a schematic of pure NaPO₃ glass in Figure 14A. Although PO₄³⁻ are tetrahedra in the glass, we have chosen to represent them with triangles in 2d space. As in the glass, most phosphate tetrahedra

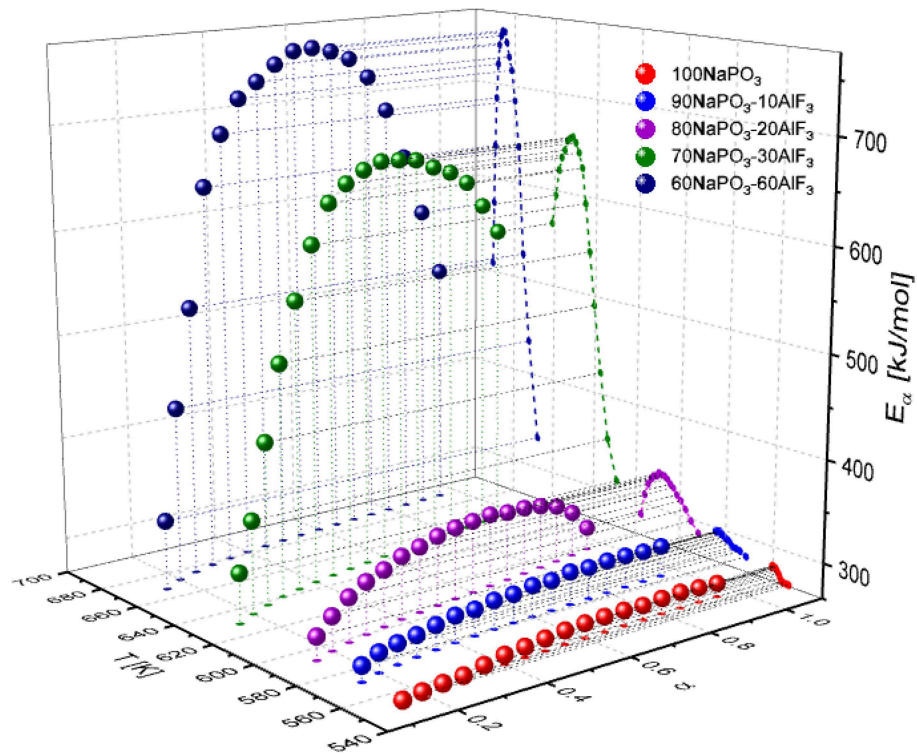


FIGURE 11 | Conversion and temperature dependence of the activation energy for NAPF [(100-x)NaPO₃-AlF₃, x = 0, 10, 20, 30, 40] glasses.

are Q^2_{0Al} species and the average phosphate chain length is five tetrahedra (grouped in yellow). This is a relatively long chain length and represents a large cooperatively rearranging region (grouped in yellow), calculated to have volume of ~ 70 nm³ in **Figure 14Aa** (≈ 4 nm in effective diameter, or 10^3 phosphate tetrahedra, using molar volume Le et al., 2017). As CRR was defined earlier, we expect each phosphate chain to be able to rearrange independently of its environment. Despite some variation in chain length, the individual tetrahedra in the phosphate chains experience very similar bonding environments and the E_a required to plastically deform each chain is roughly equal. Consequently, the glass transition is dominated by one process with a relatively low E_a of 300 kJ/mol (**Figure 11**).

Addition of AlF₃ results in the formation of Al(OP)₄F₂ groups (Bradt Müller et al., 2018) causing a sufficient increase in the degree of molecular cooperativity to raise the activation energy barrier slightly, compared with sodium metaphosphate glass. Although the connectivity of the pure phosphate backbone is decreasing, the P^2_{0Al} are being replaced by P^1_{0Al} , P^2_{1Al} , and P^3_{1Al} (**Figure 2**) maintaining the number of BOs per tetrahedra and bonding to Al, which in turn, is connected to four other phosphorus atoms through bridging oxygens (as Al(OP)₄F₂) (Bradt Müller et al., 2018). In terms of connectivity, Al(OP)₄F₂ may be considered as a Q^4 species, thus we argue that the introduction of AlF₃ increases the connectivity of the glass, which agrees with the higher activation energy observed for 10–20 mol% AlF₃ in **Figure 11**. Moreover,

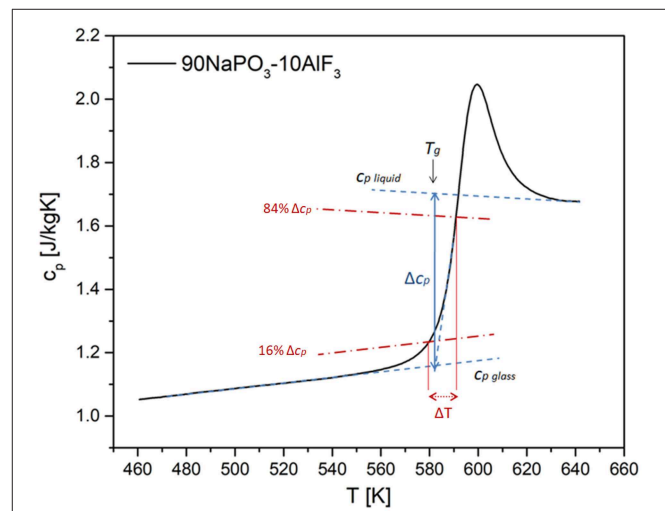


FIGURE 12 | Scheme for the determination of the quantities needed for the calculation of the CRR volume based on specific heat measurements using DSC.

there has been evidence that the introduction of halides encourages reforming of BOs from NBOs (Baasner et al., 2014); halides' bonding preference for modifiers is sufficiently strong so that the halides pull the modifiers from the phosphate backbone. In the case of $x = 20$, activation energy values

are a bit higher compared to that of $x = 10$, due to increased connectivity *via* more heteronuclear BOs between phosphate tetrahedra (Al—O—P), some bridging fluorines (Al—F—Al) and possibly some reformed P—O—P bonds as well.

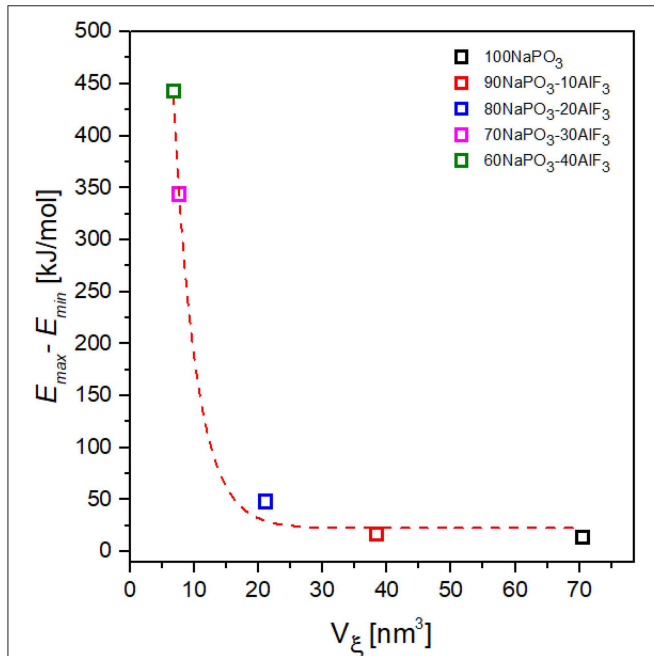
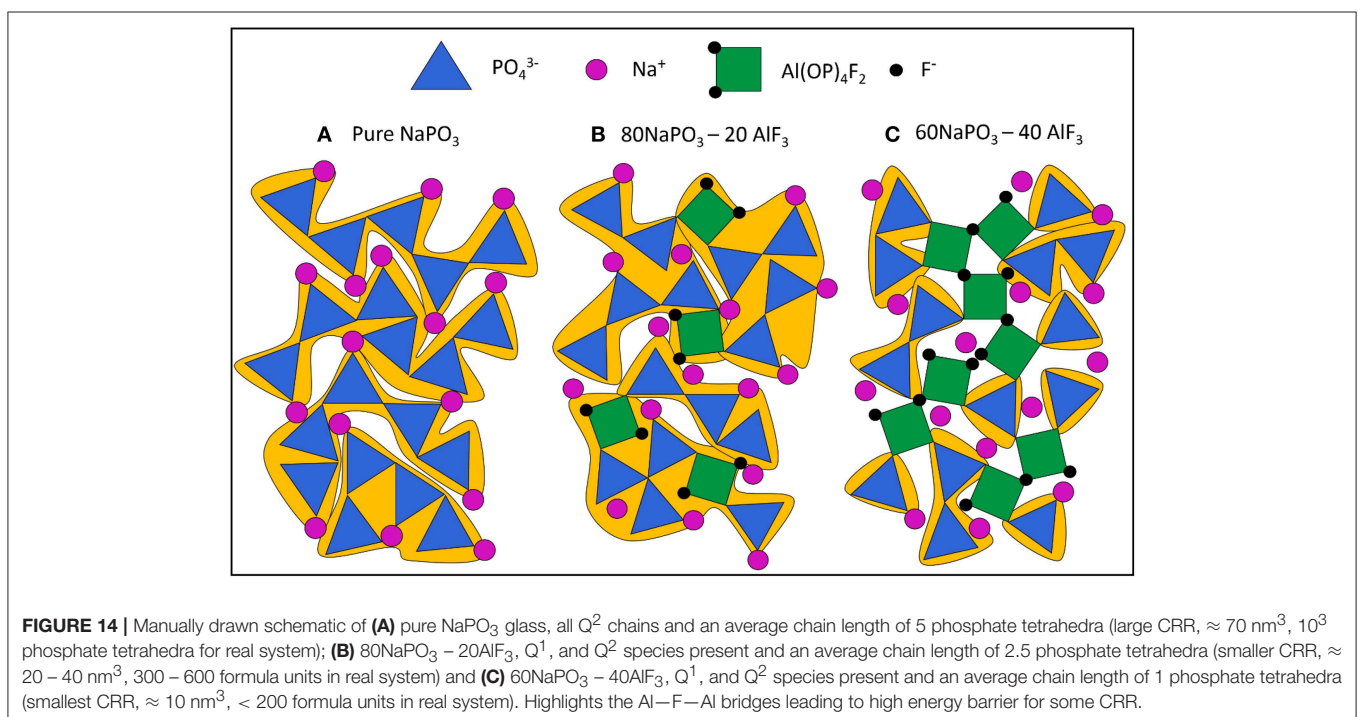


FIGURE 13 | Dependence of the activation energy variability on CRR volume for NAPF [(100- x)NaPO₃ - x AlF₃, $x = 0, 10, 20, 30, 40$] glasses.

In addition to increasing connectivity, Al(OP)₄F₂ is significantly more constrained than only Q² phosphate chains. The glass transition involves energy on the scale of plastic deformation and the Al(OP)₄F₂ octahedra can be thought as *pin* defects between phosphate chain segments. Nonetheless, the *average* phosphate chain length is much lower, 2.5 tetrahedra (grouped in yellow), making the calculated average CRR volume smaller as well (≈ 20 – 40 nm³, corresponding to some 300–600 formula units of glass).

At the highest AlF₃ content, in **Figure 14C**, we introduce some bridging fluorines between Al(OP)₄F₂ octahedra. More AlF₃ results in further depolymerization of the phosphate backbone, but also the creation of more substantial grain-boundary-like AlF₃ chains. Here the CRRs (grouped in yellow) are very small (≈ 10 nm³, < 200 formula units). The structural ensemble is becoming more heterogeneous in terms of the selective precipitation of super-structural units; the Al(OP)₄F₂ octahedra are significantly more constrained (more than four bridges to neighboring Al or P) than phosphate tetrahedra (less than two bridges to neighboring Al or P). This is similar to the structurally and dynamically heterogeneous domains found by Moesgaard et al. (2010) in calcium aluminosilicate: regions of highly constrained, alternating AlO₄ and SiO₄ tetrahedra located between more mobile, depolymerized calcium SiO₄ domains. As Brow (Brow, 1992) discusses, AlF₃ addition creates strong Al—O—P bonds, while simultaneously producing unconstrained terminal phosphorus-bound and aluminum-bound F⁻. As such, we expect that in contrast to highly constrained Al(OP)₄F₂ octahedra, there are also highly mobile phosphate regions with terminal fluorines.

A high AlF₃:NaPO₃ ratio ($x = 30, 40$) results in a large increase in activation energy (up to 700 kJ/mol) and a large



difference between the minimum and the maximum of the activation energy (450 kJ/mol). Interestingly, in **Figure 11** the activation energy minima remain relatively constant as AlF_3 is introduced (increasing from ~ 275 to 325 kJ/mol), indicating that a similar relaxation process is present in all samples which involves the pure NaPO_3 component; when we assign the minimum E_a mode to P^2_m phosphate chains, with or without Al or F^- neighbors, there appear to be only small differences based on the chemical identity of neighbors with number of constraints being the dominant factor.

At $x \geq 30$, a major structural change occurs; the aluminum-bound fluorine bridges (Al—F—Al) become more common than the phosphorus-bound terminal fluorines ($\text{P—F}\cdot(\text{Na}^+)_n$) and more BOs per phosphate tetrahedron are formed, leading to a sharp increase in the connectivity of the glass structure. According to the results shown in **Figure 11**, increase in temperature (conversion) up to around $\alpha = 0.5$ enhances molecular motion and increases the degree of molecular cooperativity leading to an increase in activation energy. Since the $\text{Al}(\text{OP})_4\text{F}_2$ is highly constrained, all the neighboring phosphate chains need to be mobile before the $\text{Al}(\text{OP})_4\text{F}_2$ participates cooperatively. As a result, the rearrangement of the regions involving $\text{Al}(\text{OP})_4\text{F}_2$ lag behind those composed of mostly phosphate chains, but also have higher activation energies (stronger Al—O—P bonds). As α increases from 0.5 to 1, the free volume continues to increase and the bonds become weaker and longer, decreasing the activation energy of the relaxation processes as well as giving polyhedra more freedom of motion, resulting in higher probabilities of less cooperative motion.

The exact size or length of the two heterogeneous domains, $\text{Al}(\text{OP})_4\text{F}_2$ octahedra and phosphate tetrahedra chains, is not known, however based on the ^{19}F , we expect mostly isolated $\text{Al}(\text{OP})_4\text{F}_2$ octahedra at low AlF_3 and as more AlF_3 is introduced, $\text{Al}(\text{OP})_4\text{F}_2$ octahedra form dimers, followed by longer $\text{Al}(\text{OP})_4\text{F}_2$ octahedra “chains” (larger domain size). Consequently, at low AlF_3 content, the isolated $\text{Al}(\text{OP})_4\text{F}_2$ octahedra domains are much shorter than the phosphate chains. Yet, at high AlF_3 content, half of the phosphate groups are no longer in chains, but are isolated pyrophosphate groups ($\text{Q}^1, \text{P}_2\text{O}_7^{4-}$). If we assume each $\text{Al}(\text{OP})_4\text{F}_2$ octahedra has two F^- bonds and that no Al—O—Al bonds form, the ^{19}F NMR informs us that at high AlF_3 content, roughly half of the $\text{Al}(\text{OP})_4\text{F}_2$ octahedra bond to another $\text{Al}(\text{OP})_4\text{F}_2$ octahedron (dimers or longer “chains”); therefore, the sizes of the two domains [$\text{Al}(\text{OP})_4\text{F}_2$ octahedra and phosphate tetrahedra] overlap and are much more comparable at high AlF_3 content. This similarity in domain size may be another reason for Al—F—Al bonding being such a crucial factor in determining the thermal relaxation behavior.

The structural schematics presented in **Figure 14** demonstrate clearly the decrease in CRR, however, they less accurately portray the structural relaxation with increasing temperature. Although $\text{Al}(\text{OP})_4\text{F}_2$ octahedra separate the glass network into differently sized phosphate regions, when the glass relaxes, the phosphate regions do not relax completely, leaving frozen $\text{Al}(\text{OP})_4\text{F}_2$ regions behind. We believe that this is more akin to lower aluminum-to-phosphorus regions cooperatively

rearranging, followed by regions with higher aluminum-to-phosphorus ratios. This creates a topologically heterogeneous glass composed of faster (low E_a) and slower (high E_a) relaxing regions. We believe these higher E_a relaxation modes to govern macroscopic properties other than the T_g ; shear and bulk modulus also increase non-linearly for samples with $\geq 30\%$ AlF_3 content (without the commensurate non-linear increase in molar volume, packing density or volume density of bonding energy; Le et al., 2017).

CONCLUSION

^{31}P NMR indicated that the introduction of AlF_3 increases the average connectivity in the glass through heteronuclear Al—O—P bonding, i.e., replacement of $\text{P}^2_{0\text{Al}}$ with $\text{P}^2_{1\text{Al}}$ and formation of $\text{P}^3_{1\text{Al}}$ at high AlF_3 content, and the forced association of Na^+ with terminal fluorines. ^{19}F NMR revealed that AlF_3 adds to the phosphate backbone mostly as $\text{Al—F}\cdot(\text{Na}^+)_n$, with initial AlF_3 addition creating $\text{P—F}\cdot(\text{Na}^+)_n$ bonds until the lack of sodium and availability of aluminum force Al—F—Al bonds to become more dominant at 30 mol% AlF_3 . DFT calculations verified the ^{19}F assignments, lack of Al—F—P bonds and the strong coordination of Na^+ with *both* bridging and terminal fluorine. In agreement with other ^{27}Al NMR results, we found that low Al/P ratio or high fluorine content result in Al[6] sites being the dominant species negligible Al[5] and Al[4] sites at high AlF_3 content; based on Bradtmüller et al.'s. [15] investigation, we conclude that our system also contains octahedral $\text{Al}(\text{OP})_4\text{F}_2$. Finally, we used Valence Unit theory to explain the instability of Al—F—P bonds, while demonstrating the preference for Al[6]—F—Al[6]; similarly, we used V.U. theory to discuss the role of sodium in the formation of $\text{P—F}\cdot(\text{Na}^+)_n$ and Al[4]—F—Al[4] bonds.

Multinuclear NMR analysis allowed us to produce structural schematics that demonstrate the structural and topological differences which occur as a function of AlF_3 and relate the trends to relaxation processes. Concurrent with the rise in maximum E_a , the variability of the E_a for the glass transition also increases with increasing AlF_3 content. We proposed that there are phosphate-rich regions which are more like NaPO_3 without many bridging bonds to Al, but at the same time, there are $\text{Al}(\text{OP})_4\text{F}_2$ -rich regions that are much more topologically constrained. As more AlF_3 is added, some glass regions become increasing constrained due to more Al—F—Al and Al—O—P cross-links, which increases further ΔE_a . At the same time, $\text{P—F}\cdot(\text{Na}^+)_n$ bonds create less constrained, flexible regions that have similarly low E_a as phosphate chains in pure NaPO_3 . The large difference between minimum and maximum E_a indicates that the glass transition is composed of several different-energy structural relaxation processes and that the glass structure is heterogeneous on the length-scale of these processes.

Surprisingly, despite a higher maximum E_a for relaxation processes and a higher connectivity in the glass network at high AlF_3 content, an on average smaller volume of cooperatively rearranging regions is found for glasses with higher

fluorine content. The $\text{Al}(\text{OP})_4\text{F}_2$ octahedra are significantly more topologically constrained and break up the phosphate network into smaller phosphate chains, similar to pin defects in granular materials. The observed decrease in the *average* CRR size agrees with the results from ^{31}P NMR: the average homonuclear phosphate chain length decreases with increasing AlF_3 content (mostly $\text{P}^2_{1\text{Al}}$ at high AlF_3).

DATA AVAILABILITY

All datasets generated for this study are included in the manuscript and/or the supplementary files.

AUTHOR CONTRIBUTIONS

CC, LW, JP, and UW-Z conceived and planned the experiments. JP (thermal analysis) and UW-Z (NMR) performed the

experiments, processed the experimental data and performed the analysis. JZ planned and carried out simulations. QL manufactured the samples. LW, CC, QL, UW-Z, JP, and JZ contributed to the interpretation of the results. CC took the lead in writing the discussion and manuscript with contributions from all authors. All authors provided critical feedback and helped shape the research, analysis and manuscript.

FUNDING

This project has received funding from the European Research Council (ERC) under the European Union's Horizon 2020 research and innovation program (ERC grant UTOPEs, grant agreement no. 681652). CC is grateful to the Natural Sciences and Engineering Research Council of Canada (NSERC) for financial support.

REFERENCES

- Adam, G., and Gibbs, J. H. (1965). On the temperature dependence of cooperative relaxation properties in glass-forming liquids. *J. Chem. Phys.* 43, 139–146. doi: 10.1063/1.1696442
- Baasner, M., Hung, I., Kemp, T. F., Dupree, R., Schmidt, B. C., and Webb, S. L. (2014). Constraints on the incorporation mechanism of chlorine in peralkaline and peraluminous $\text{Na}_2\text{O}-\text{CaO}-\text{Al}_2\text{O}_3-\text{SiO}_2$ glasses. *Am. Mineral.* 99, 1713–1723. doi: 10.2138/am.2014.4717
- Benzine, O., Bruns, S., Pan, Z., Durst, K., and Wondraczek, L. (2018). Local deformation of glasses is mediated by rigidity fluctuation on nanometer scale. *Adv. Sci.* 5:916. doi: 10.1002/adv.201800916
- Bradt Müller, H., Zhang, L., de Araujo, C. C., Eckert, H., Möncke, D., and Ehrle, D. (2018). Structural studies of $\text{NaPO}_3-\text{AlF}_3$ glasses by high-resolution double-resonance NMR spectroscopy. *J. Phys. Chem. C* 122, 21579–21588. doi: 10.1021/acs.jpcc.8b06162
- Brow, R. K. (1992). A multinuclear MAS NMR study of the short-range structure of fluorophosphate glass. *J. Mater. Res.* 7:1892. doi: 10.1557/JMR.1992.1892
- Brow, R. K., Kirkpatrick, R. J., and Turner, G. L. (1993). Nature of alumina in phosphate glass: II, Structure of sodium aluminophosphate glass. *J. Am. Ceram. Soc.* 76, 919–928. doi: 10.1111/j.1151-2916.1993.tb05316.x
- Bunker, B. C., Kirkpatrick, R. J., and Brow, R. K. (1991). Local structure of alkaline-earth boroaluminate crystals and glasses: I, Crystal chemical concepts—structural predictions and comparisons to known crystal structures. *J. Am. Ceram. Soc.* 29, 1425–1429. doi: 10.1111/j.1151-2916.1991.tb04123.x
- Champagnon, B., Wondraczek, L., and Deschamps, T. (2009). Boson peak, structural inhomogeneity, light scattering and transparency of silicate glasses. *J. Non. Cryst. Solids* 355, 712–714. doi: 10.1016/j.jnoncrysol.2009.01.029
- Donth, E. (1982). The size of cooperatively rearranging regions at the glass transition. *J. Non. Cryst. Solids* 53, 325–330. doi: 10.1016/0022-3093(82)90089-8
- Donth, E.-J. (2001). *The Glass Transition: Relaxation Dynamics in Liquids and Disordered Materials*. Berlin: Springer-Verlag. doi: 10.1007/978-3-662-04365-3
- Duval, E., Mermet, A., and Saviot, L. (2007). Boson peak and hybridization of acoustic modes with vibrations of nanometric heterogeneities in glasses. *Phys. Rev. B - Condens. Matter Mater. Phys.* 75, 1–9. doi: 10.1103/PhysRevB.75.024201
- Ediger, M. D. (2000). Spatially heterogeneous dynamics in supercooled liquids. *Annu. Rev. Phys. Chem.* 51, 99–128. doi: 10.1146/annurev.physchem.51.1.99
- Flynn, J. H., and Wall, L. A. (1966). A quick, direct method for the determination of activation energy from thermogravimetric data. *J. Polym. Sci. B Polym. Lett.* 4, 323–328. doi: 10.1002/pol.1966.110040504
- Friedman, H. L. (2007). Kinetics of thermal degradation of char-forming plastics from thermogravimetry. Application to a phenolic plastic. *J. Polym. Sci. Part C Polym. Symp.* 6, 183–195. doi: 10.1002/polc.5070060121
- Garn, P. D. (1990). Kinetics of thermal decomposition of the solid state. II. Delimiting the homogeneous-reaction model. *Thermochim. Acta* 160, 135–145. doi: 10.1016/0040-6031(90)80254-V
- Greaves, G. N., and Ngai, K. L. (1995). Reconciling ionic-transport properties with atomic structure in oxide glasses. *Phys. Rev. B* 52, 6358–6380. doi: 10.1103/PhysRevB.52.6358
- Greaves, G. N., and Sen, S. (2007). Inorganic glasses, glass-forming liquids and amorphizing solids. *Adv. Phys.* 56, 1–166. doi: 10.1080/00018730601147426
- Hempel, E., Hempel, G., Hensel, A., Schick, C., and Donth, E. (2000). Characteristic length of dynamic glass transition near T_g for a wide assortment of glass-forming substances. *J. Phys. Chem. B* 104, 2460–2466. doi: 10.1021/jp991153f
- Kresse, G., and Furthmüller, J. (1996). Efficient iterative schemes for ab initio total-energy calculations using a plane-wave basis set. *Phys. Rev. B* 54, 11169–11186. doi: 10.1103/PhysRevB.54.11169
- Kresse, G., and Joubert, D. (1999). From ultrasoft pseudopotentials to the projector augmented-wave method. *Phys. Rev. B* 59, 1758–1775. doi: 10.1103/PhysRevB.59.1758
- Le, Q. H., Palenta, T., Benzine, O., Griebenow, K., Limbach, R., Kamitsos, E. I., et al. (2017). Formation, structure and properties of fluoro-sulfo-phosphate poly-anionic glasses. *J. Non. Cryst. Solids* 477, 58–72. doi: 10.1016/j.jnoncrysol.2017.09.043
- MacKenzie, K. J. D., and Smith, M. E. (2002). Multinuclear solid-state NMR of inorganic materials. *Pergamon Mater. Ser.* 6, 3–727. doi: 10.1016/j.jaap.2008.03.002
- Massiot, D., Fayon, F., Capron, M., King, I., Le Calvé, S., Alonso, B., et al. (2002). Modelling one- and two-dimensional solid-state NMR spectra. *Magn. Reson. Chem.* 40, 70–76. doi: 10.1002/mrc.984
- Moeller, R. P., Gupta, P. K., Elterman, P. B., Moynihan, C. T., Sasabe, H., Macedo, P. B., et al. (2006). Structural relaxation in vitreous materials. *Ann. N. Y. Acad. Sci.* 279, 15–35. doi: 10.1111/j.1749-6632.1976.tb39688.x
- Moesgaard, M., Keding, R., Skibsted, J., and Yue, Y. (2010). Evidence of intermediate-range order heterogeneity in calcium aluminosilicate glasses. *Chem. Mater.* 15, 4471–4483. doi: 10.1021/cm1011795
- Möncke, D., da Neto, M. C. B., Bradtmüller, H., de Souza, G. B., Rodrigues, A. M., Elkholy, H. S., et al. (2018). $\text{NaPO}_3-\text{AlF}_3$ glasses: fluorine evaporation during melting and the resulting variations in structure and properties. *J. Chem. Technol. Metall.* 53, 1047–1060. Available online at: <https://dl.uctm.edu/journal/web/j2018-6>
- O'Reilly, J. M. (1977). Conformational specific heat of polymers. *J. Appl. Phys.* 48, 4043–4048. doi: 10.1063/1.323444

- Ozawa, T. (1965). A new method of analyzing thermogravimetric data. *Bull. Chem. Soc. Jpn.* 38, 1881–1886. doi: 10.1246/bcsj.38.1881
- Perdew, J. P., Burke, K., and Ernzerhof, M. (1996). Generalized gradient approximation made simple. *Phys. Rev. Lett.* 77, 3865–3868. doi: 10.1103/PhysRevLett.77.3865
- Pickard, C. J., and Mauri, F. (2001). All-electron magnetic response with pseudopotentials: NMR chemical shifts. *Phys. Rev. B* 63:245101. doi: 10.1103/PhysRevB.63.245101
- Vyazovkin, S. (2001). Modification of the integral isoconversional method to account for 699 variation in the activation energy. *J. Comput. Chem* 22, 178–183. doi: 10.1002/1096-987X(20010130)22:2<178::AID-JCC5>3.0.CO;2-%23
- Vyazovkin, S. (2006). Model-free kinetics: staying free of multiplying entities without necessity. *J. Therm. Anal. Calorim.* 83, 45–51. doi: 10.1007/s10973-005-7044-6
- Vyazovkin, S. (2015). *Isoconversional Kinetics of Thermally Stimulated Processes*. London: Springer. doi: 10.1007/978-3-319-14175-6
- Vyazovkin, S. (2016). A time to search: finding the meaning of variable activation energy. *Phys. Chem. Chem. Phys.* 18, 18643–18656. doi: 10.1039/C6CP02491B
- Vyazovkin, S. (2018). “Chapter 4: Modern isoconversional kinetics,” in *Handbook of Thermal Analysis and Calorimetry - Recent Advances, Techniques and Applications*, 2nd ed, eds S. Vyazovkin, N. Koga, and C. Schick (Amsterdam: Elsevier), 131–172.
- Wondraczek, L., and Behrens, H. (2007). Molar volume, excess enthalpy, and Prigogine-Defay ratio of some silicate glasses with different (P,T) histories. *J. Chem. Phys.* 127:2794745. doi: 10.1063/1.2794745
- Wondraczek, L., Behrens, H., Yue, Y., Deubener, J., and Scherer, G. W. (2007). Relaxation and glass transition in an isostatically compressed diopside glass. *J. Am. Ceram. Soc.* 90, 1556–1561. doi: 10.1111/j.1551-2916.2007.01566.x
- Zhang, L., De Araujo, C. C., and Eckert, H. (2007). Structural role of fluoride in aluminophosphate sol-gel glasses: high-resolution double-resonance NMR studies. *J. Phys. Chem. B* 111, 10402–10412. doi: 10.1021/jp072725w
- Zhang, Y., Yang, G., and Yue, Y. (2013). Calorimetric signature of structural heterogeneity in a ternary silicate glass. *J. Am. Ceram. Soc.* 96, 3035–3037. doi: 10.1111/jace.12562

Conflict of Interest Statement: The authors declare that the research was conducted in the absence of any commercial or financial relationships that could be construed as a potential conflict of interest.

Copyright © 2019 Calahoo, Petrovic, Le, Werner-Zwanziger, Zwanziger and Wondraczek. This is an open-access article distributed under the terms of the Creative Commons Attribution License (CC BY). The use, distribution or reproduction in other forums is permitted, provided the original author(s) and the copyright owner(s) are credited and that the original publication in this journal is cited, in accordance with accepted academic practice. No use, distribution or reproduction is permitted which does not comply with these terms.